# Design and characterization of an oxides hybrid dispersion strengthened iron based composite with a graded and architectural microstructure

Kaoutar Naji, Maya Marinova, Matthieu Touzin, Ph Pouligny, Marie-Noëlle Avettand-Fènoël

# Design and characterization of an oxides hybrid dispersion strengthened iron based composite with a graded and architectural microstructure.

K. Naji[a,b], M. Marinova[c], M. Touzin[a], Ph. Pouligny[b], M.-N. Avettand-Fènoël[a,*]

[a] Univ. Lille, CNRS, INRA, ENSCL, UMR 8207 - UMET - Unité Matériaux et Transformations, 59000 Lille, France
[b] SNCF Réseau, Direction Ingénierie et Projets, 93574 la Plaine Saint Denis, France
[c] Institut Chevreul, University of Lille & CNRS, Villeneuve d'Ascq 59655, France

* corresponding author

## Abstract

A graded Fe based composite reinforced with tetragonal yttria stabilized zirconia, monoclinic zirconia, ~~and~~ wüstite and at a less extent, $Zr_{0.978}Fe_{0.022}O_{1.978}$ (~~T~~tetragonal) and $Zr_{0.85}Y_{0.15}O_{1.93}$ (~~C~~cubic) was developed by high energy ball milling, compaction and sintering. ~~Some other phases such as $Zr_{0.978}Fe_{0.022}O_{1.978}$ (T) and $Zr_{0.85}Y_{0.15}O_{1.93}$ (C) were also put into evidence in the bulk material~~. Solid state sintering entailed (i) the growth of Fe grains which remained submicrometric and (ii) the coarsening of oxides reinforcements forming an interconnected network in the bulk graded composite. ~~The weak reinforcement matrix bonds originate the fracture of the bulk material during bending tests. The bulk composite presents a slight graded hardness, but the gradation is less marked than expected because of the presence of a network of coarsened reinforcements. Regarding the electrical conductivity, its gradation along the bulk composite is finally noted.~~
The increase of oxide reinforcements volume fraction enabled to obtain a material with a graded electrical resistivity and a slightly graded hardness; the bending resistance of the as-developed material was however decreased because of the weakness of the reinforcements – matrix bonds.

## Keywords

A. Metal matrix composite; B. Mechanical alloying; B. Sintering; C. Microstructure; C. Mechanical properties; C. Electrical conductivity~~; D. Metallography; D. Thermal analysis; D. Scanning electron microscopy; D. Transmission electron microscopy; D. X-ray diffraction~~.

## 1. Introduction

Because of the ever increasing demand that requires materials with combined performing functional and mechanical properties to meet specifications of industrial applications, various metallic matrix based composites (MMCs) have been developed. Numerous examples, such as $Y_2O_3$ reinforced W based composites **[1-2]**, metallic glass reinforced Al composites **[3]**, Cu/Nb composites **[4]** are for instance reported. Various reviews devoted to the topic, among which **[5-9]**, can be cited. A peculiar kind of MMCs is further concerned by the graded MMCs **[10]**. These materials present a graded microstructure with, for instance, an increasing volume fraction of reinforcements along the material. This architecture confers them an evolution of their mechanical and/or functional properties. The graded MMCs can be developed by various processes which proceed either (i) at the liquid state such as casting, electroslag refining, spray forming, additive manufacturing, thermal spraying, or (ii) at the solid state like natural sintering, hot isostatic pressing, spark plasma sintering, friction stir processing or accumulative roll bonding etc.

The present study is a first step in the design of a graded Fe based composite for a railways application which requires an evolution of both mechanical properties (hardness) and electrical resistivity. The ticklish choice of the powdered reinforcements nature has been dictated by various specifications, namely (i) their great electrical resistivity, (ii) their Young modulus close to that of Fe of 211 GPa, (iii) their thermal expansion coefficient close to that of Fe of 12.1 (14.6)$\times 10^{-6}$ $C^{-1}$ over [20-100°C] ([20-800°C]) **[11]**, (iv) their thermal stability for a pretty large range of temperatures and (v) their absence of solubility in Fe. 3 mol.% yttria stabilized zirconia (YSZ) in the tetragonal crystal lattice (with a stoichiometry of $Y_{0.02}Zr_{0.98}O_{1.99}$) was chosen as reinforcement since it presents an

electrical conductivity of $10^{-9}$ MS/m at 600°C **[12]**, the highest fracture toughness among all the other crystalline structures **[13]** and a Young modulus of 205 GPa. YSZ also presents a coefficient of thermal expansion of 6-8.8$\times 10^{-6}$ °C$^{-1}$ **[14],** which should not entail too many thermal stresses during the cooling stage of MMC elaboration. Besides YSZ has a large negative energy of formation, which is very likely close to that of $ZrO_2$ equal to -1042.2 kJ at 27°C and to -818.2 kJ at 1227°C **[11]** or lower than that of $ZrO_2$, by comparison with other literature results **[15]**; its melting temperature amounts to 2700°C and its tetragonal lattice structure is maintained up to 2360°C **[~~15~~16]**, which suggests its thermal stability. In addition, the diffusion coefficients of Zr and Y in Fe are respectively $2\times10^{-16}$ m²/s and $5\times10^{-18}$ m²/s at 977°C **[~~16~~17]**, implying that coarsening should not be expected during MMC elaboration. Zr and Y further present a very low solubility in the Fe matrix **[11]**, $Y_2O_3$ presents no solubility in Fe at least at 1000 and 1200°C **[~~17~~18]** and $ZrO_2$ and Fe are not soluble at 1000°C **[~~18~~19]**. YSZ should then pin Fe grain boundaries provided it experiences ~~no coarsening~~ a very restrained coarsening process **[20]**. A graded oxide dispersion strengthened Fe based MMC was thus developed by powder metallurgy, namely high energy ball milling, compaction and sintering. The current paper aims (i) to characterize the microstructure of the graded MMC and to identify the mechanisms of formation of the microstructure, (ii) to characterize the mechanical and electrical properties of the graded MMC and (iii) to correlate the microstructure with the mechanical and electrical properties of the graded MMC.

## 2. Experimental procedure

Iron (polygonal morphology, bimodal particle size distribution with 2 average modes of 5 and 20 µm, and purity of 98%) and 3 mol.% yttria stabilized zirconia (YSZ) (spherical morphology with a tendency to form agglomerates because of hygroscopic properties, monomodal particle size distribution with a mode of 200 nm, and purity of 99%) powders were milled in various proportions to obtain Fe - X vol.% YSZ ~~composite~~ blends with X = 0, 5, 10, 20, 30 or 40. Milling was performed under argon (with an oxygen content lower than 2 ppm and a water content lower than 3 ppm) for 100 hours in a Fritsch Pulvérisette 6$^{TM}$ planetary milling system made of stainless steel with a vial and seven 10 diametered balls. The ball-to-powder weight ratio and the vial rotational speed were respectively 4:1 and 727.2 rpm. The composite blends were then uniaxially compacted under 1600 MPa for 5 min and green compacts with a diameter of 10 mm and a thickness of 1.5 mm were obtained. The composite subparts with an incremental volume fraction of reinforcements were subsequently stacked and sintered in a free radial stresses matrix at 1250°C for 1 hour under a uniaxial pressure of 50 kPa and secondary vacuum (2.6 $\times 10^{-7}$ atm), the heating and cooling rates being equal to 10°C/min.

In order to investigate their microstructure, the composite powdered blends were dispersed, embedded in a mounted carbon resin and polished up to 1 µm while the sintered materials were cut and polished up to 1 µm. Nital solution enabled to etch the Fe grain boundaries in the sintered composites.

The microstructure of the milled powders and of the sintered material was characterized by light microscopy, and by scanning electron microscopy (SEM) by means of a JSM 7800F, JEOL® microscope with secondary electrons (SE) or back scattering electrons (BSE) mode and X-ray energy dispersive spectroscopy (~~EDX~~ EDS). Thin foils sampled in both (i) the inner of a Fe-40 vol.% YSZ milled powder particles mounted in carbon resin and (ii) the graded bulk composite have been prepared by focused ionic beam in a FEI Strata DB 235 microscope with a double beam. They were analyzed by transmission electron microscopy (TEM) with a FEI Tecnai G2 20 microscope equipped with ~~EDX~~ EDS spectrometer and a FEI Titan Themis 300 microscope. The Tecnai G2 microscope has a $LaB_6$ filament and operates at 200 kV. The TITAN Themis 300 S/TEM is equipped with a probe aberration corrector and monochromator, allowing special resolution of 70 pm and energy resolution of 150 meV. The microscope has also a super-X windowless 4 quadrant SDD (silicon drift detector) detection system for the STEM ~~EDX~~EDS mapping and several annual dark field detectors. The experiment has been performed at 300 kV with spot size 9, semi-convergence angle of 21 mrad and probe current of approximately 100 pA. For the high angle annular dark field (HAADF) images, collection angles were between 50 mrad and 200 mrad. For the STEM-EELS (Electron Energy Loss

Spectroscopy) experiment, the excitation of the monochromator has been set at 0.6 allowing energy resolution of 140 meV at the zero loss peak. The semi-convergence angle was 15 mrad and the collection angle was 49 mrad.
In order to identify the nature of phases, X-ray diffraction (XRD) analyses were performed at room temperature in a Philips X'Pert Pro® equipment using a Bragg-Brentano configuration and a Co anticathode with a wavelength of 1.78901 Å. An in-situ XRD experiment using a Bragg-Brentano configuration and a Cu anticathode with a wavelength of 1.54056 Å was also carried out with a D8 HTK1200N apparatus on the Fe-40 vol.% YSZ composite under primary vacuum to identify the nature of phase transformations during heating. The heating rate was 10°C/min and XRD patterns were recorded periodically each 50°C from 400 to 800°C and each 25°C from 800 to 1150°C.
Some dilatometry tests and differential scanning calorimetry analyses were also carried out to get additional data about these phase transformations. Dilatometry tests were performed on the Fe-40 vol.% YSZ composite in a horizontal dilatometer DIL 402C, Netzsch® using the sintering thermal cycle under primary vacuum. Differential scanning calorimetry (DSC) analyses on the Fe-40 vol.% YSZ powder were carried out in a calorimeter DSC 404C, Netzsch®; the milled composite powder was heated at 10°C/min up to 1350°C under argon flow.
The geometrical density of the green compact was calculated; the density of the sintered material, as well as the open and closed porosities contents were measured by Archimede's method according to NF ISO5017 standard **[~~19~~20~~2~~1]** using absolute ethylic alcohol.

With regard to the mechanical properties, Vickers microhardness tests under a load of 25 g for 15 s were performed on each sub-composite part of the sintered graded material.
Some 3 points static bending tests were also carried out according to NF EN ISO 14125 standard **[~~20~~21~~2~~22]** on 10 mm diametered and 15 mm long graded bulk MMCs in which the central part contained 40 vol.% YSZ while the YSZ content decreased from the central part towards the cylinder bases. The upper mechanical support was a 5 mm diametered cylinder whose speed was 1 mm/min. It has been applied on the central part of the graded material. The 2 lower mechanical supports were fixed at a distance of 3.25 mm from the centre of the graded material. The load applied on the upper mechanical support was in-between 100 N and 20 kN.

The electrical conductivity of each sub-composite part was finally measured by the Van der Pauw method **[~~21~~22~~2~~23]**. The latter method consists in joining 4 Cu wires with the sintered composite material by means of silver lacquer. An electrical current is introduced between 2 of these 4 Cu wires while the voltage is measured between the 2 remaining wires so as to calculate the electrical conductivity of the composite.

# 3. Results

## 3.1. Fe matrix crystallite/grain size

Sintering led to the growth of the nanometric Fe grains generated by ball milling. Indeed the Fe crystallite size is in-between 5 and 15 nm in the Fe-40 vol.% YSZ milled powder (see yellow boundaries in figure 1a) while the Fe-40 vol.% YSZ sintered material presents some Fe grains with a mean size close to 500 nm (figure 1b and c).

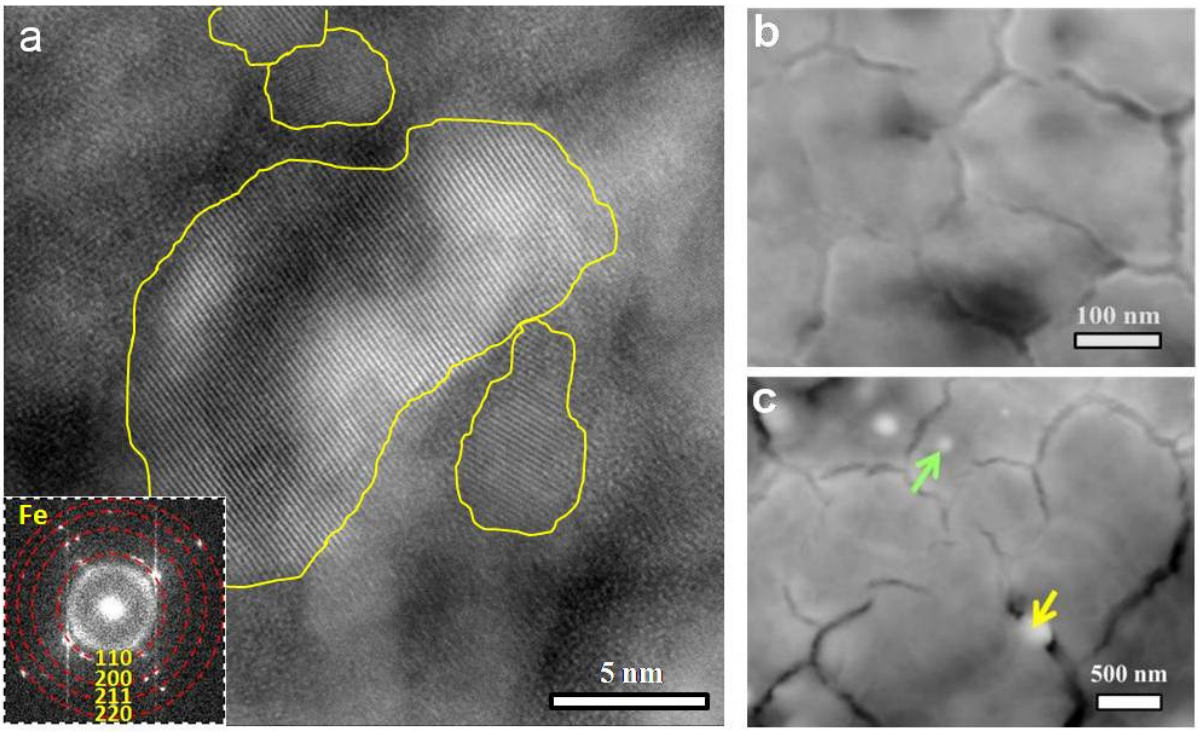

Figure 1: Fe grain size in a Fe-40 vol.% YSZ milled polycrystalline powder particle (High Angular Annular Dark Field (HAADF) image with Fast Fourier Transform (FFT) pattern of Fe (a), and in the sintered Fe-40 vol.% YSZ bulk material etched with nital (BSE/SEM) (b and c).

### 3.2. Reinforcements

#### 3.2.1. Reinforcements distribution

*Comparison between the Fe-40 vol.% YSZ milled powder and the Fe-40 vol.% YSZ bulk material* - The Fe – 40 vol.% YSZ milled powder is made of composite particles which present a very fine dispersion of reinforcements, as displayed in figure ~~2a to l, n to o~~2a to n, p to q. Their size is lower than 200 nm and many present a mean size of 20 nm; their spacing is lower than 100 nm as shown in the dark field images depicting some monoclinic zirconia and YSZ reinforcements (figures 2 ~~j, k, l and o~~l, m, n and q). After sintering, the bulk Fe-40 vol.% composite is composed of a Fe matrix together with a network (at least in 2 dimensions) of few micrometers sized coarse reinforcements (figure ~~2q to s~~2s to u). These reinforcements are either intergranular (yellow arrow in figure 1c) or intragranular (green arrow in figure 1c). Some reinforcements with a rounded shape can be very fine (0.1 to 2 µm) (see yellow and green arrows in figure 1c and black arrows in figure 2~~s~~u). It is worthy to note that the finest ones present the same shape and size as those of the elemental YSZ particles. In BSE mode (figures ~~2q, r and s~~2s, t and u), different contrasts can be noted and are directly linked to the chemical nature of the phases, namely a bright contrast linked to YSZ reinforcements, a light grey contrast related to Fe grains and a dark grey contrast linked to iron oxide phases, which will be presented in §3.2.2.

*Microstructure of the graded bulk composite* – Figure 3 displays the graded architecture of the second phases in the bulk composite constituted of the different composite subparts, each containing X vol. % YSZ with X over the range [0-40]. An interconnected network of reinforcements can be noticed through the global graded bulk composite (figure 3) like that observed in the Fe-40vol.% YSZ bulk composite subpart (figure 2~~g~~u). In addition, the pressure applied during sintering enabled to get porosity free interfaces between the various subparts of the sintered material (see rectangular zones in figure 3 which show the localization of the initial interfaces between the various subparts). The location of these well-bonded interfaces has been able to be identified thanks to the presence at the bulk material periphery of very small zones, where there was a lack of bonding between the different

subparts. ~~No~~Neither evolution of porosity content nor change of the shape and size of the spherical finest reinforcements has been noticed along the graded composite.

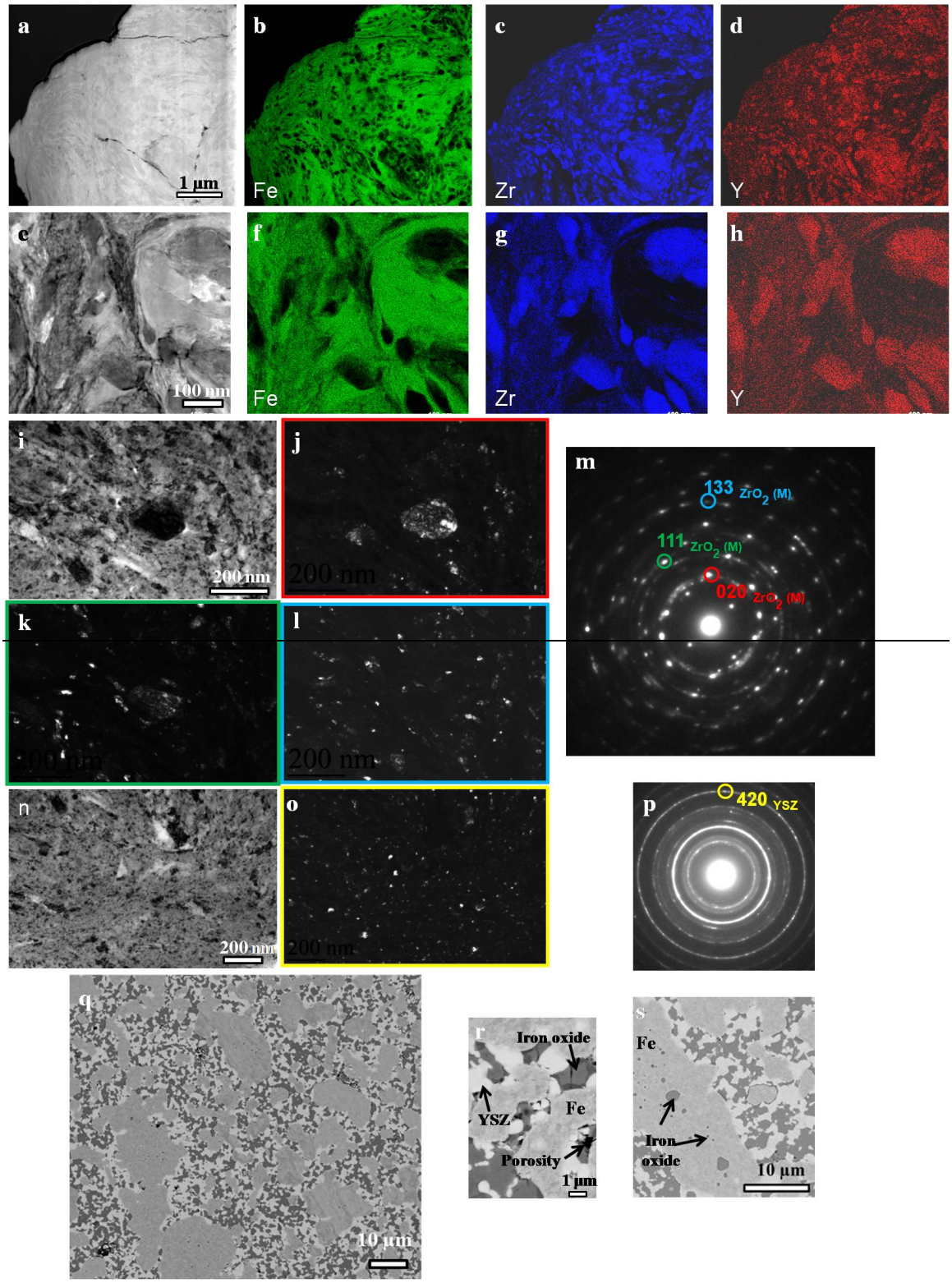

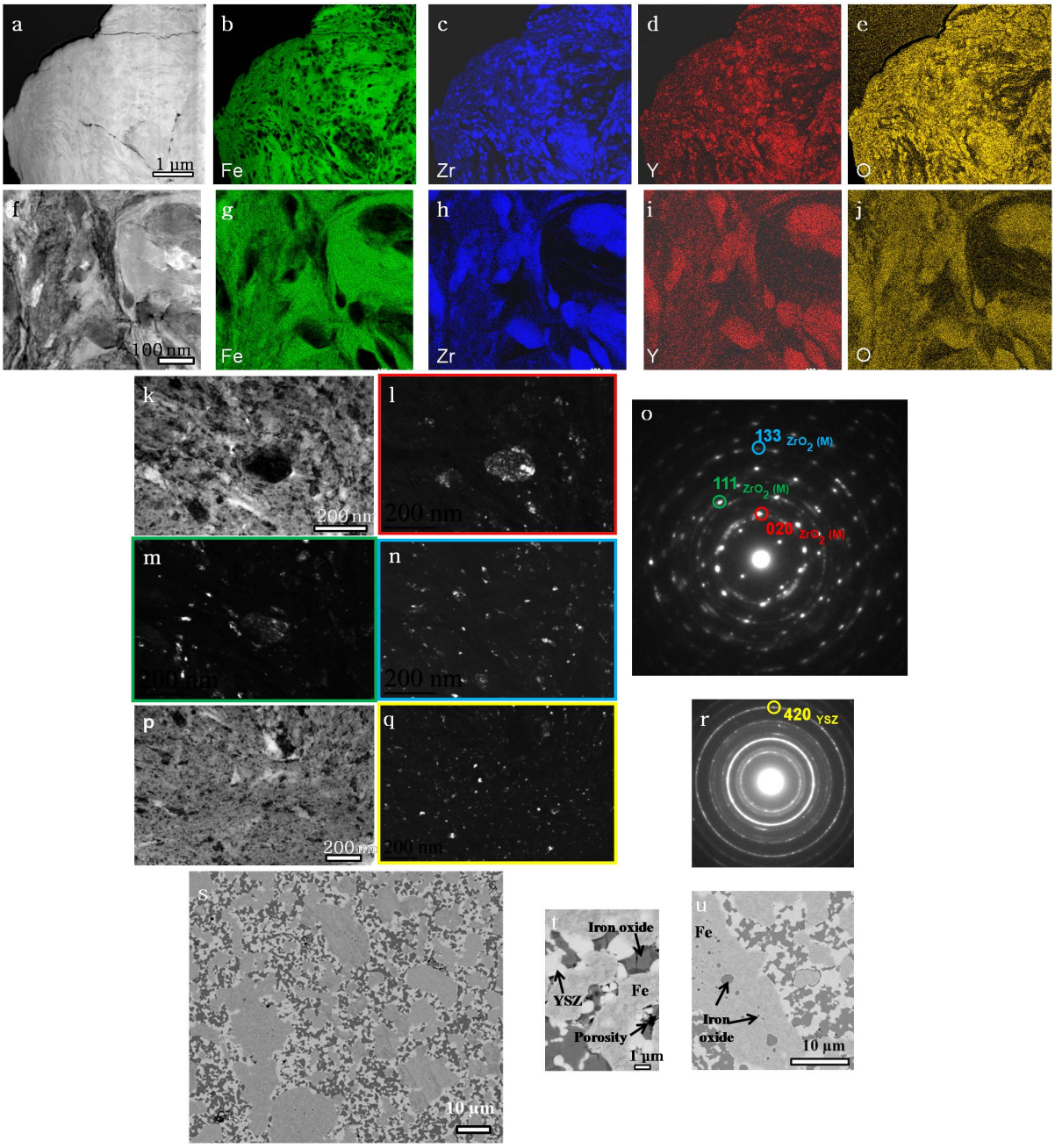


Figure 2: Distribution of the reinforcements in the inner of Fe-40 vol.% YSZ milled particles: HAADF-STEM image (a) and respective X-ray maps of Fe $K_\alpha$, Zr $K_\alpha$ ~~and,~~ Y $K_\alpha$ and O $K_\alpha$ (~~EDX~~EDS-STEM) (b to ~~d~~e); HAADF-STEM image at a finer scale (~~e~~f) and respective X-ray maps of Fe $K_\alpha$, Zr $K_\alpha$ ~~and,~~ Y $K_\alpha$ and O $K_\alpha$ (~~EDX~~EDS-STEM) (~~f~~g to ~~h~~j); bright field TEM image (~~i~~k) and dark field TEM images (~~j, k and l~~l,m and n) linked to the colored spots in the electron spot diffraction pattern (~~m~~o); bright field TEM image (~~n~~p) and dark field TEM image (~~o~~q) linked to the colored spot in the electron spot diffraction pattern (~~p~~r).

Details of the inner of the bulk Fe-40 vol.% YSZ sintered composite (BSE/SEM) (~~q to s~~s to u).

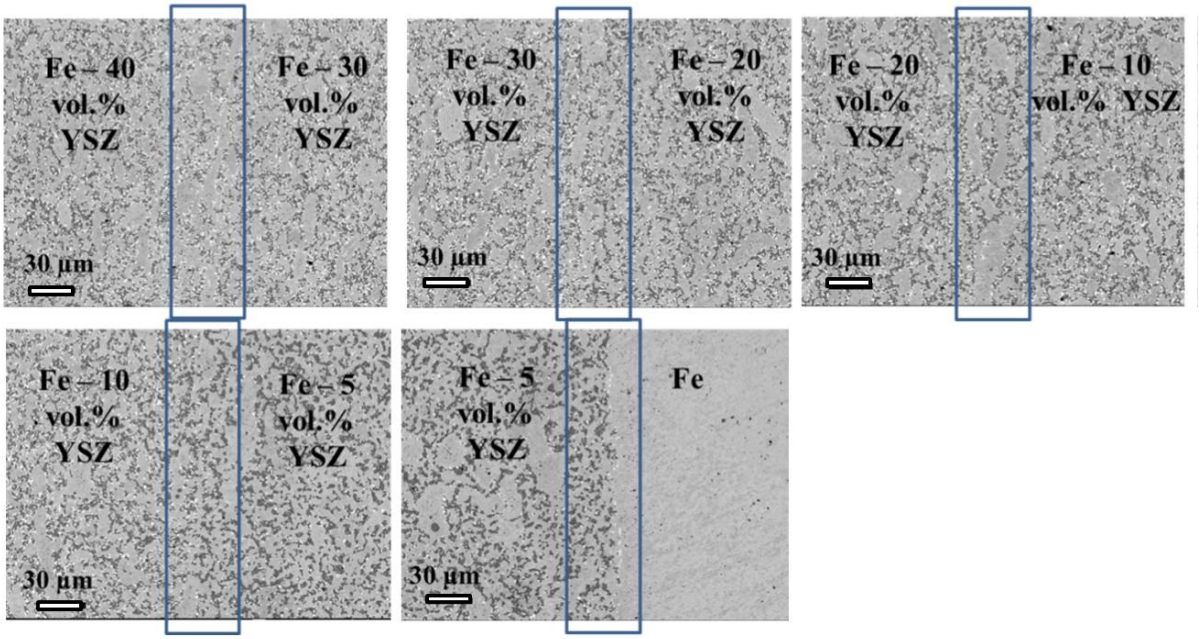


Figure 3: Graded architecture of the second phases in the bulk composite (BSE/SEM). The blue rectangles surround the localization of the initial interfaces between the different subparts of the graded sintered material.

### 3.2.2. Nature of reinforcements

*Comparison between the Fe-40 vol.% YSZ milled powder and the Fe-40 vol.% YSZ bulk material –*
X-ray diffraction pattern of the milled powder depicted in figure 4 shows that the Fe-40 vol.% YSZ milled powder consists of, beside Fe α, monoclinic (M) $ZrO_2$ (also observed by TEM (figure 2 ~~i to mk~~ to o)), tetragonal (T) (also observed by TEM (figure 2 ~~n to pp~~ to r)) and/or cubic (C) YSZ (their Bragg peaks are so close that it is difficult to determine with accuracy the crystal structure of YSZ), and $Fe_3O_4$. The latter phase together with $Fe_2O_3$ was also detected by Raman spectroscopy and X-ray Photoelectron Spectroscopy (not presented here). Concerning the sintered sample, it presents the same nature of phases as the milled powder and the Bragg peaks of these phases are better defined since the phases are well crystallized (figure 4). An additional phase, namely FeO, is however also put into evidence in the sintered sample (figure 4). An increase of the monoclinic $ZrO_2$ phase is also noted after sintering.

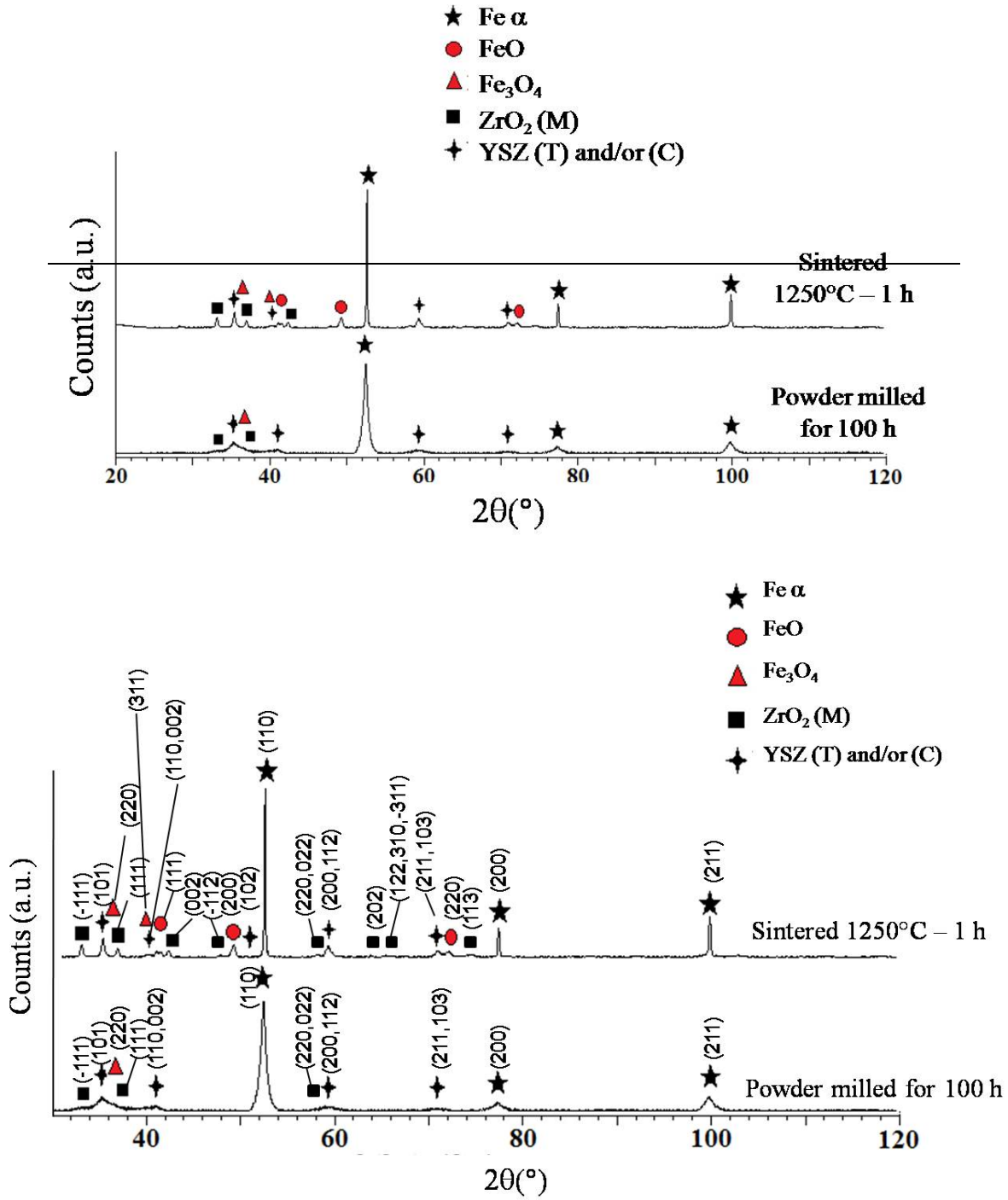


Figure 4: X-ray diffraction patterns of Fe-40 vol.% YSZ composite after milling and sintering. C, T and M abbreviations are respectively used for cubic, monoclinic and tetragonal crystal structures.

*Phase transformations during sintering* – Dilatometry (figure 5a) and differential scanning calorimetry (figure 5b) were respectively performed on the Fe-40 vol.% YSZ green compact and milled powder to detect the onset temperature of phase transformations occurring during sintering and to identify the endothermal or exothermal feature of these phase transformations. Three phase transformations were noted in the dilatogram, namely at 540°C (blue arrow in figure 5a), at 770°C (green arrow in figure 5a) and at 940°C with a marked contraction (black arrow in figure 5a). Figure 5b further indicates that the first one is exothermal (blue arrow in figure 5b), the second one is endothermal (green arrow in figure 5b) and the third one endothermal (black arrow in figure 5b). The dilatogram also indicates that some shrinkage occurs at 1050°C (red arrow in figure 5a). Some other

events marked respectively by orange and grey arrows are noted in the DSC pattern (figure 5b) at temperatures close to 1210 and 1330°C. The marked endothermal event occurring at 1330°C is very likely due to melting of a phase or to eutectic transformation.

In addition and in order to identify the nature of the phase transformations, in-situ X-ray diffraction patterns were recorded during heating, up to 1150°C and at a heating rate of 10°C/min. Their comparison highlighted the occurrence of phase transformations at temperatures (i) between 500 and 550°C with the attenuation of the intensity of $Fe_3O_4$ Bragg peaks and the formation of FeO (blue circles in figure 6), (ii) between 600 and 650°C with Feα → Feγ (green circles in figure 6), and (iii) near 950°C with $ZrO_2$ (M) → $ZrO_2$ (T) (the 2 dimensional map of in-situ XRD over [800-1150°C] range is not presented here). The temperatures of phase transformations are consistent with those supplied by dilatometry and DSC experiments. It is worthy to note that the contraction due to allotropic transformation of Fe is almost not visible in figure 5a. The event at 770°C may correspond to the completion of the allotropic transformation of Feα → Feγ (figure 6), which is known to be endothermal **[~~23~~24]**. In addition, the monoclinic to tetragonal transformation of zirconia leads to a contraction as depicted in figure 5a and is an endothermal reaction, as already indicated in literature **[~~22-2324-25~~25-26]**. However no phase transformation could have been identified ~~neither~~ at a temperature ~~close to 770°C (green arrow in figure 5) with in-situ XRD experiment (figure 6), nor at~~ of 1210°C. The endothermal signal at 1330°C (grey arrow in figure 5b) very likely corresponds either to ($ZrO_2$ + FeO → liquid) eutectic transformation occurring at 1332°C or to FeO melting occurring at 1371°C in equilibrium conditions **[~~24~~2627]**.

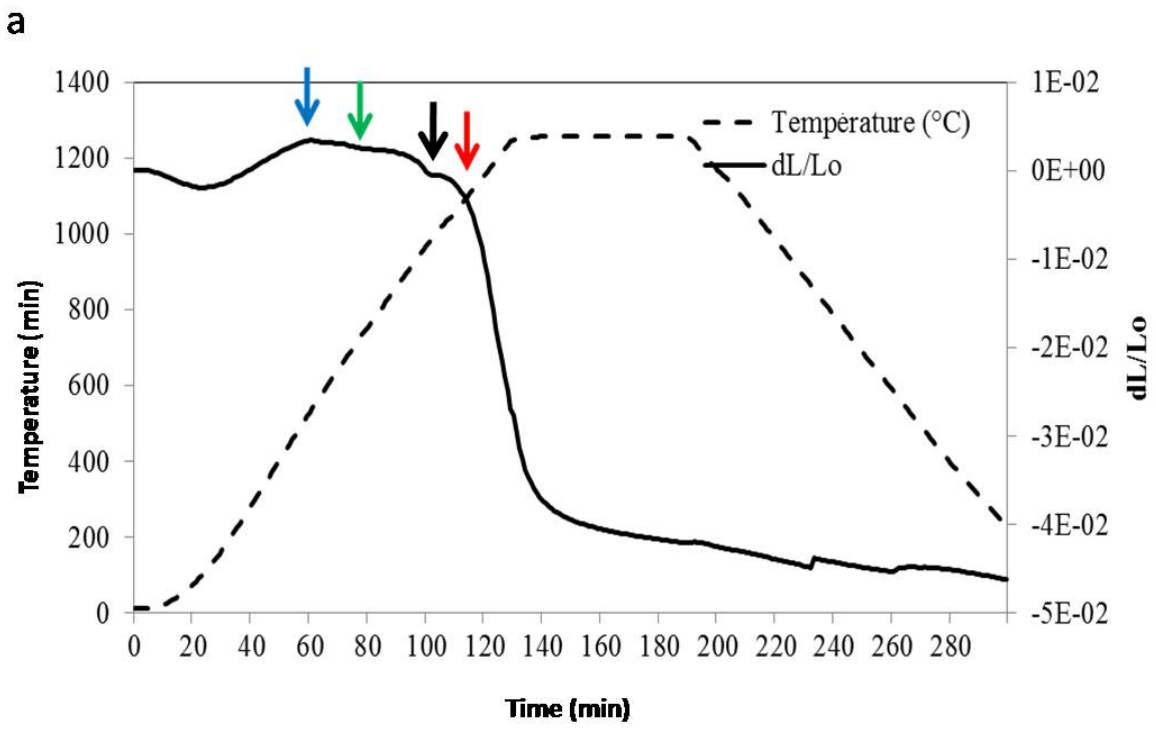

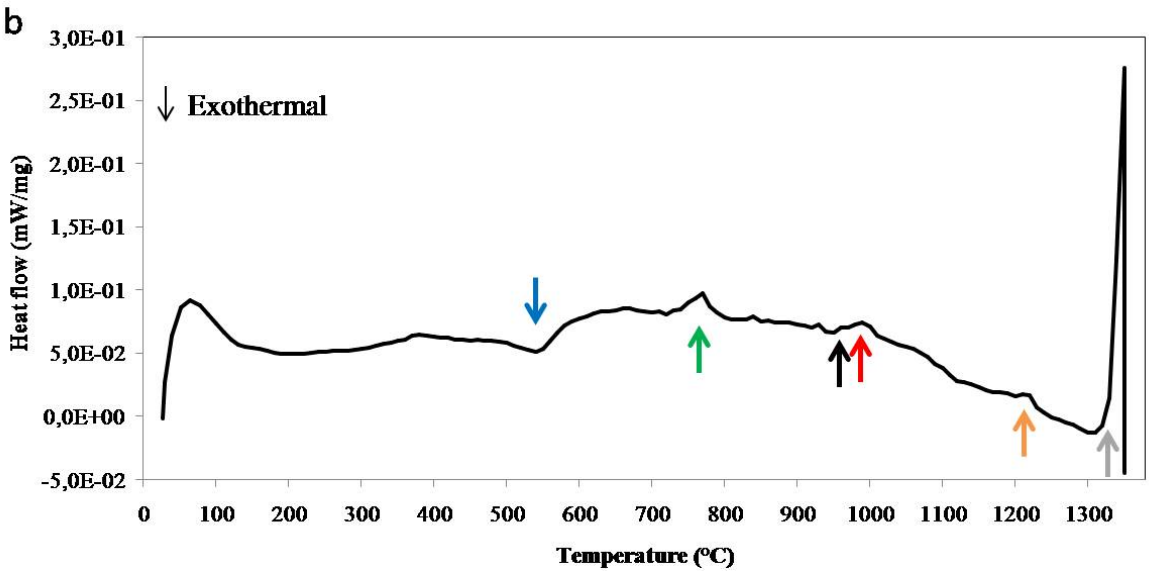


Figure 5: a) Thermal cycle and dilatogram of a green compact of milled Fe-40 vol.%YSZ powder and b) differential scanning calorimetry pattern of the milled Fe-40 vol.%YSZ powder during heating at a heating rate of 10°C/min. The first part of the dilatogram and of the DSC curve is very likely due to the inertia of furnace.

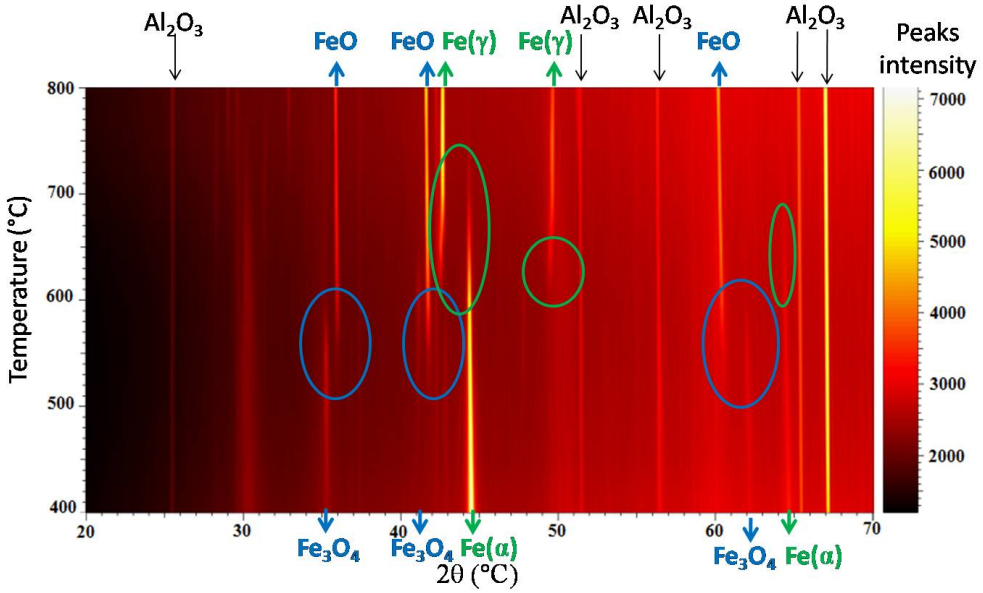


Figure 6: Example of the two dimensional map showing the Bragg peaks positions and their intensities (see color bar) *vs.* the temperature range of [400-800°C] (in-situ XRD analysis of the Fe-40 vol.% YSZ blend with a heating rate of 10°C/min and a step of 50°C). Alumina signal results from the backing plate.

*Identification of local phases at the atomic scale in the sintered material* - Some local phases were also identified by HAADF/STEM (figure 7). They deal with $ZrO_2$ (M), $Zr_{0.978}Fe_{0.022}O_{1.978}$ (T) and $Zr_{0.85}Y_{0.15}O_{1.93}$ (C). Their chemical composition was confirmed by ~~EDX~~EDS analyses (not presented here). Some twins (not presented here) have been observed in $ZrO_2$ (M), which suggests that it results from the phase transformation $ZrO_2$ (T) → $ZrO_2$ (M) occurring during the cooling stage of sintering. The latter phase transformation is indeed known to be accompanied by twinning during cooling **[~~222~~425]**. The FeO phase has finally been identified next to zirconia (figure 8e) and at the $Fe_3O_4$-Fe interface (figure 8f and g). EELS spectra from the areas shown in figure 8g are given in panel h of the

same figure. An energy shift is observed towards higher energies, which indicates a change of oxidation state towards $Fe^{3+}$. This is a clear evidence of the presence of both FeO and $Fe_3O_4$.

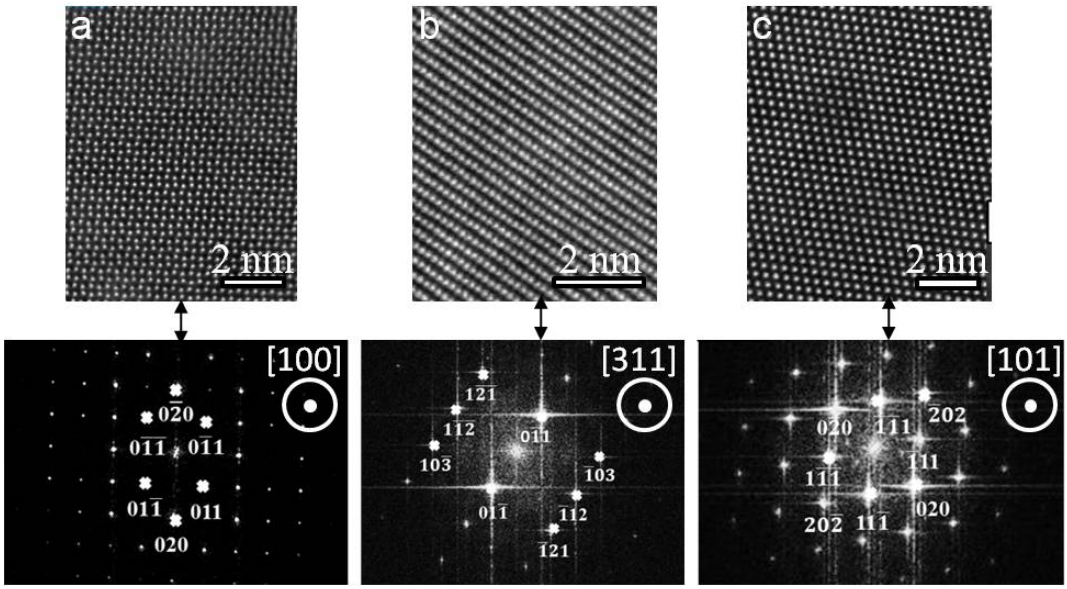


Figure 7: HAADF-STEM micrographs of sintered Fe-40 vol.% YSZ: atomic arrangements and Fast Fourier Transform (FFT) patterns of a) $ZrO_2$ (M), b) $Zr_{0.978}Fe_{0.022}O_{1.978}$ (T) and c) $Zr_{0.85}Y_{0.15}O_{1.93}$ (C).

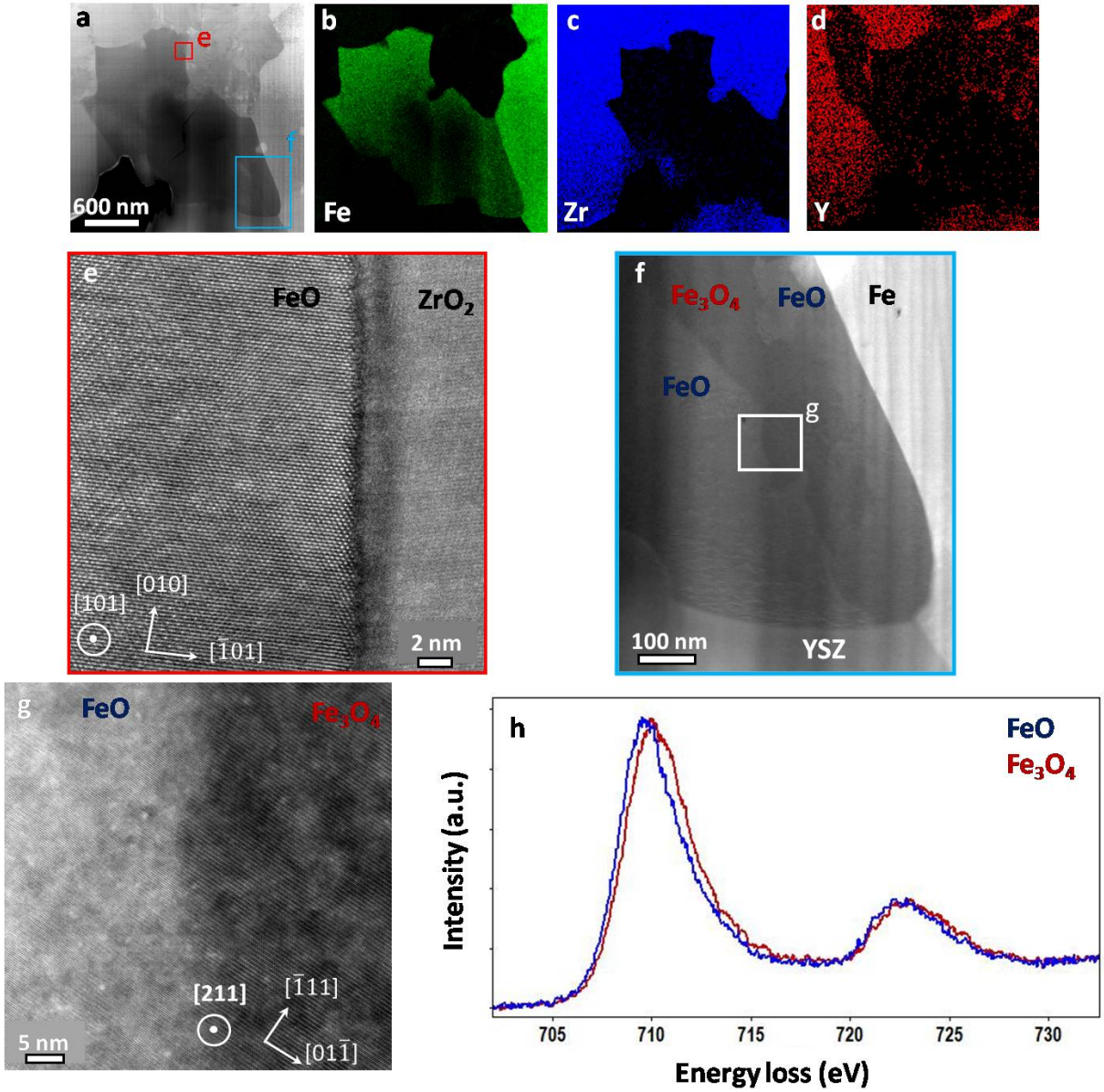


Figure 8: HAADF-STEM image of Fe – 40 vol.% YSZ sintered material (a) and respective X-ray maps of Fe $K_\alpha$, Zr $K_\alpha$ and Y $K_\alpha$ (~~EDX~~EDS-STEM) (b to d). e) and f) are respective magnifications of red and blue encircled zones in figure a. The white encircled area in figure f is magnified in panel g, and associated EELS spectra are shown in panel h.

### 3.2.3. Volume fraction of phases

Table 1 compares the volume fractions of the phases contained in the Fe-40 vol.% YSZ blend after milling and after sintering. The estimation by the Rietveld method of the phases volume fractions in the milled powder is quite ticklish because of the very large Bragg peaks which present a low intensity and which can be convoluted. It can be noted that the amount of both Fe and FeO after sintering almost corresponds to that of Fe before sintering while the proportion of monoclinic $ZrO_2$ and of YSZ after milling evolves during sintering.

According to inductively coupled plasma (ICP) analyses, the oxygen content in the milled Fe-40 vol.% YSZ powder amounts to 10.10 mass.% while the calculated oxygen content of this mixture before milling was equal to 8.53 mass.%. In addition, the estimation of the oxygen content in the sintered Fe-40 vol.% YSZ composite from the data of Table 1 leads to an oxygen content of 10.96 mass.%. These calculations prove that there was some contamination by oxygen during milling (very likely because of a lack of hermeticity of the vial for a long milling time despite its conditioning under

argon) and sintering. The contamination by oxygen very likely also occurred during the handling and use of powders under air between the processing and analyzing steps.

Table 1: Volume fractions of phases after milling and after sintering for the Fe-40 vol.% YSZ blend according to Rietveld method. The uncertainty of the values is close to 0.05.

| Phase | Fe | FeO | $ZrO_2$ monoclinic (M) | YSZ tetragonal (T) | $Fe_3O_4$ and $Fe_2O_3$ |
|---|---|---|---|---|---|
| After milling | ~0.61 | ~0 | ~0.13 | ~0.26 | Difficult to estimate |
| After sintering | 0.47 | 0.22 | 0.18 | 0.13 | ~0.01 |

In addition, the volume fraction of iron oxides in the sintered composite subparts is similar whatever the amount of zirconia based reinforcements in the subpart.

### 3.3. Density of the bulk sintered graded composite

Sintering improved the density of the Fe-40 vol.% YSZ composite subpart green compact of about 14.7 units. The green density amounted to 72.0% while the sintered density reached 86.7%. In addition, the sintered density of the bulk graded composite material is evaluated at 90.7% with an open porosity percentage of 2.5% and a closed porosity percentage of 6.8% according to Archimede's method. The calculation of the theoretical density of the graded material has been made taking into account the mass of each composite subpart. For the calculation, only the YSZ reinforcements were considered, which is not perfectly rigorous.

### 3.4. Electrical and mechanical properties of the bulk sintered graded composite

*Electrical conductivity* – The electrical conductivity of the composite parts is divided at least by 4 compared to that of sintered pure Fe (figure 9). In addition, the greater the YSZ content in the composite subpart, the lower the electrical conductivity is (figure 9). The electrical conductivity of the composite with the greatest YSZ content remains far greater than that of YSZ.

*Microhardness* – The results of microhardness tests are displayed in figure 9. The presence of reinforcements enables to strengthen pure iron but the different composite subparts do not see their microhardness evolve a lot with the YSZ content.

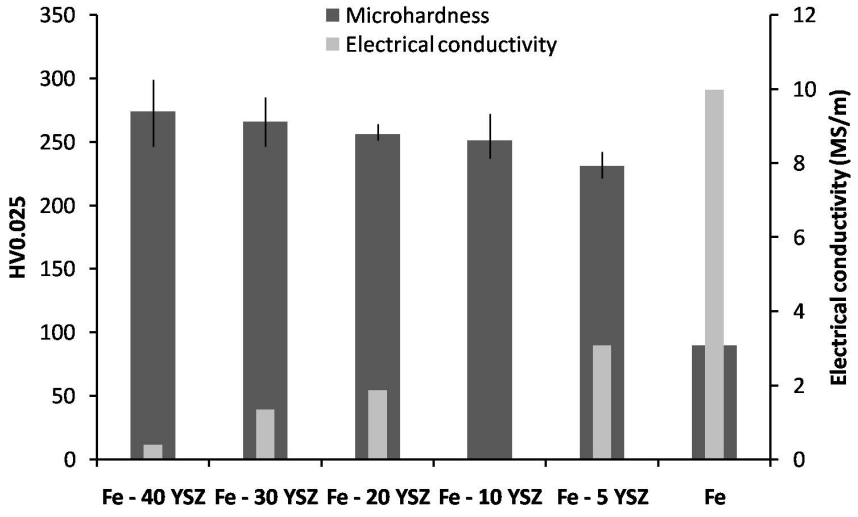


Figure 9: Microhardness and electrical conductivity of the various subparts of the bulk sintered composite.

*3 points bending properties* – According to the 3 points bending tests, the graded sample withstood a 4270 N force which generated a largest deflection of 0.85 mm in its middle before its failure. Its fracture energy, which supplies information about its toughness, amounts to 1.51 J. This low value can be explained, at least, by the incomplete densification of the material. The fracture patterns of the specimen are displayed in figure 10. Some cracks can be observed inside the reinforcements and at the interface of reinforcements and Fe matrix. The polyphased material also presents some lacks of bonding as well as porosities, which proves that densification was not complete and which confirms the density values.

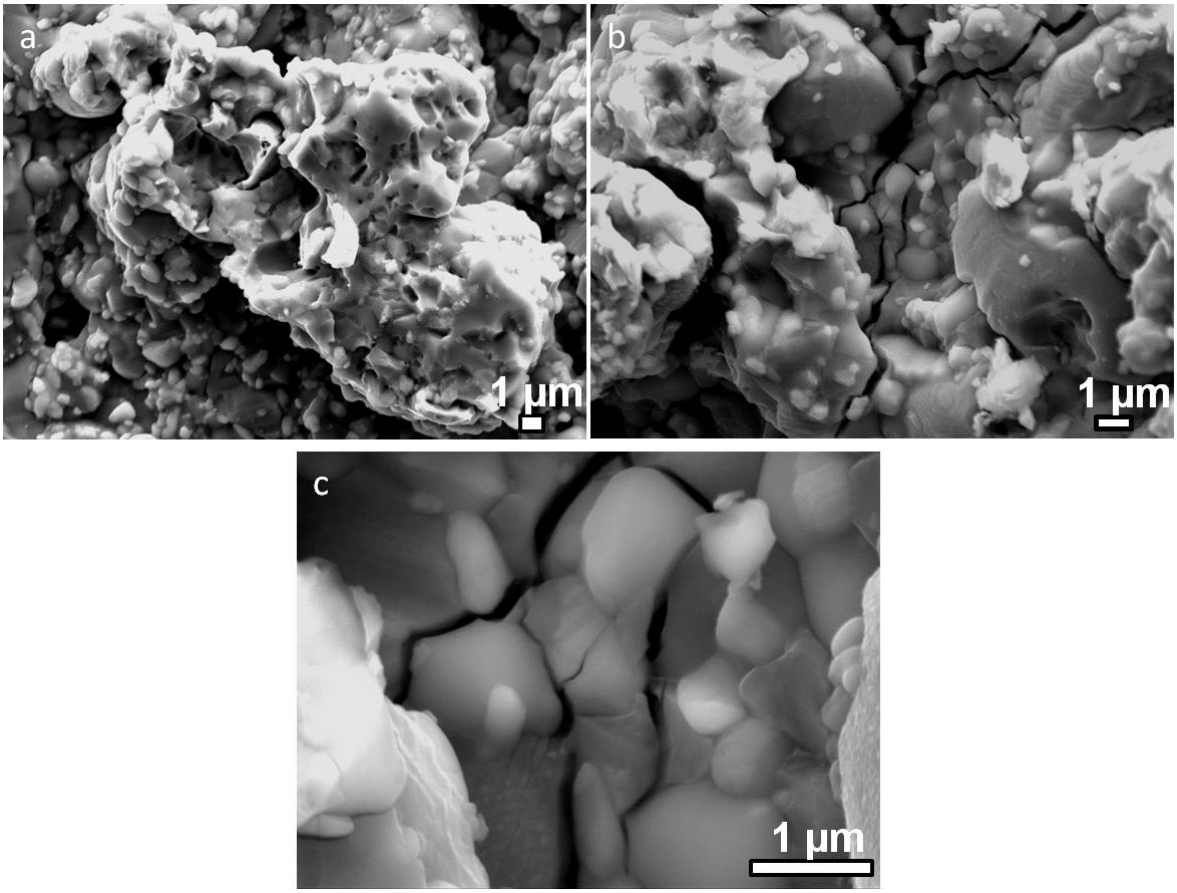

Figure 10: Fracture surface of the graded MMC after 3 points bending test (SE/SEM).

# 4. Discussion

## 4.1. Phase transformations

Various phase transformations occurred during sintering of the graded composite leading to the formation of hybrid reinforcements.

*Allotropic transformation of Fe* – According to dilatometry (figure 5a) and X-ray diffraction analyses (figure 6), the allotropic transformation of Fe occurs at a temperature in-between 600 and 650°C. It is worth noting that this temperature is far lower than the equilibrium point of 910°C **[11]**. This can very likely be explained by the nanometric mean size close to 5-15 nm of the Fe crystallites in the milled powders (figure 1a) and by the strain induced in the powders during high energy ball milling which enables to reduce the required energy to achieve the transformation **[~~28~~29]**.

*Phase transformations of $ZrO_2$ and YSZ* – An increase of the volume fraction of the monoclinic zirconia at the expense of tetragonal YSZ was observed in the sintered material compared to the milled powders (Table 1). This suggests a destabilization of tetragonal YSZ during sintering. During heating, Y and/or Fe contained in zirconia network may have diffused outside the YSZ network leading to a $Y_2O_3$ or $Fe_2O_3$ content, lower than that required of 3 mol.% **[~~22~~24~~2~~5]**, to stabilize the tetragonal structure of zirconia at room temperature. This could have reduced the oxygen vacancies content introduced in the aliovalent dopants such as Y and Fe and destabilized the tetragonal YSZ **[~~22~~24~~2~~5]**. During cooling, the zirconia depleted of $Y_2O_3$ and $Fe_2O_3$ would have recovered its monoclinic structure stable at room temperature.

*Formation of ternary Zr based phases* - Tetragonal $Zr_{0.978}Fe_{0.022}O_{1.978}$ and cubic $Zr_{0.85}Y_{0.15}O_{1.93}$ have been identified (figure 7). The first phase $Zr_{0.978}Fe_{0.022}O_{1.978}$ is maintained at room temperature and seems to correspond to β-$ZrO_2$, which can contain 2.2 mol.% FeO in solid solution and exists at equilibrium over [1170-2347°C] range as mentioned in literature **[~~24~~26~~2~~7]**. FeO in solution in zirconia would thus enable to stabilize the tetragonal structure of zirconia at room temperature. In the same way, the insertion of yttria into zirconia to form $Zr_{0.85}Y_{0.15}O_{1.93}$ enabled the stabilization of the cubic structure of zirconia at room temperature, as already shown in literature **[~~1~~5~~1~~6]**.
In addition and contrary to some observations reported in literature concerned by sintering of Fe-$ZrO_2$ composites **[~~25-27~~27~~,29-30~~28,30-31]**, it is worth noting that ε-$Zr_6Fe_3O$, which appears at 900°C and results from a reaction between iron and not stabilized zirconia **[~~25-27~~27~~,29-30~~28,30-31]**, has not been detected in the sintered materials. Likewise, no Fe, Y and O bearing phase was detected in the present study unlike some results reported in literature **[~~27~~30~~3~~1]**.

*Formation of iron oxides* – After sintering, the global volume fraction of iron oxides is greater than that obtained after milling while pure Fe volume fraction is reduced (table 1). The milled Fe powders were shown to present at their surfaces $Fe_3O_4$ according to XPS and Raman analyses although milling was performed under not perfectly pure argon. In addition, Fe may also oxidize during sintering although sintering occurred under secondary vacuum and low oxygen pressure. In-situ X-ray diffraction analyses indicate that the Bragg peaks of $Fe_3O_4$ become less intense at a temperature close to 540°C while FeO is formed (figure 6). FeO is also detected at the Fe-$Fe_3O_4$ interface (figure 8f,g,h). Dilatometry and differential scanning calorimetry analyses further show that FeO is formed via an exothermal reaction. The FeO phase would thus result from the reaction of Fe with $Fe_3O_4$. This assumption is in agreement (i) with the Fe-O equilibrium phase diagram according to which the phase transformation happens at 570°C **[11]** and (ii) with thermodynamical data which indicate that the chemical reaction is exothermal and that its $\Delta_rH°$ is -75058 J/mol **[11]**. The difference of the temperatures of reaction can be explained by the nanometric features of the compacted powders.
Moreover, many FeO phases are aggregated next to zirconia rich zones (figures 2q to s and 8e) and $Fe_3O_4$ rich zones (figure 8f to h). The diffusion of $O^{2-}$ ions supplied by YSZ, which is faster than those of $Zr^{4+}$ and $Y^{3+}$ ions **[~~28~~31~~3~~2]**, and whose kinetics is high from 800°C **[~~29~~32~~3~~3]**, as well as the diffusion of $Fe^{3+}/Fe^{2+}$ from $Fe_3O_4$, which is faster than that of $O^{2-}$ **[~~28~~31~~3~~2]** may have entailed, under temperature effect, FeO formation and depletion of stoichiometric zirconia in oxygen vacancies. The latter argument would nevertheless remain to be proved.
Finally, FeO is maintained in the sintered material at room temperature (figure 4) while according to the equilibrium Fe-O phase diagram **[11]**, the Ellingham diagram **[~~30~~33~~3~~34]** and literature **[~~31~~34~~3~~5]**, stoichiometric FeO is not stable at room temperature and atmospheric pressure. Its stabilization at room temperature is however reported in literature (i) following its formation in a wet and oxidizing atmosphere **[~~32-33~~35~~-36~~36-37]**, or (ii) under high pressure **[~~34~~37~~3~~8]**, or (iii) following its elaboration by milling of Fe and $Fe_3O_4$, cold compaction under 150 MPa, sintering at 1100°C for 1 h under Ar and high isostatic pressing at 900°C for 1 h under 50 MPa under vacuum **[~~35~~38~~3~~9]** or (iv) following Fe infiltration in tetragonal yttria stabilized zirconia **[~~36~~39~~40~~]**. In the present case, FeO stability at room temperature would be explained by the fact that sintering occurs under secondary vacuum in a reducing atmosphere. The low oxygen pressure could hinder FeO dismutation into Fe and $Fe_3O_4$ during cooling.

### 4.2. Densification and sintering mechanisms

### 4.2.1. Factors promoting the densification

Two factors, namely the powders nanostructuration and the presence of iron and yttrium dopants, were gathered in order to promote the sintering kinetics ~~and then the densification~~.

*Nanostructuration and defects* – The fineness and nanostructuration of milled powders (figure 1) are actually known to favor the sintering kinetics, as already observed in literature **[~~37-38~~40-~~41~~41-42]**. During milling, the powders stored high strain energy. In addition, compaction leads to increase the density of dislocations in the powder particles. Thus the high vacancies and dislocations density favors the atomic diffusion during sintering, which accelerates the sintering kinetics.

*Dopants* – With regard to dopants, YSZ sintering is suggested to be activated by yttria dopant, which was native in the elemental powder, or by iron oxide dopant provided its content is greater than 1 mass.% **[~~39-40~~42-~~43~~43-44]**. Fe is indeed known as YSZ dopant which improves the sintering kinetics of YSZ, all the more that sintering occurs under oxygen poor atmosphere, the interstitial defects density being more important in YSZ under a low oxygen pressure **[~~41~~44445]**. ~~$Zr^{4+}$, $Y^{3+}$, $Fe^{3+}$ and $O^{2-}$ radii are respectively 0,84 Å, 1,019 Å, 0,55 to 0,78 Å, and 1,38 Å. $Fe^{3+}$ can enter into the crystal structure of zirconia and occupy either substitutional sites ($Zr^{4+}$) (if its content is greater than 1.5 mol.%) or interstitial sites (if its content is lower than 1.5%). In the first case, it reduces the YSZ crystal volume already distordaed (distorded structure of fluorite).~~ Given the Fe content in tetragonal phase of zirconia, $Fe^{3+}$ is expected to be in interstitial sites. The doping defect of $Fe^{3+}$ promotes the jumps frequency of $Zr^{4+}$. $Fe^{3+}$ is indeed expected to migrate via a mechanism of vacancies diffusion during sintering. In addition, ~~$Fe^{3+}$ radius (0.55 to 0.78 Å) is smaller than $Zr^{4+}$ one (0.84 Å),~~ its insertion in $ZrO_2$ lattice weakens the resistance of Zr-O bonds and the activation energy for $Fe^{3+}$ diffusion is lower than those of $Zr^{4+}$ and $Y^{3+}$. This entails an increase of diffusion coefficient of $Zr^{4+}$ and of its diffusion speed, which promotes YSZ sintering kinetics **[~~42~~45~~46~~46]**.

However, the reached density for the (graded) composite (§3.3) was lower than expected, which is explained in the following part (§ 4.2.2).

### 4.2.2. Factors hindering the densification and sintering mechanisms

#### 4.2.2.1. Density

Sintering of the Fe-40 vol.% YSZ composite enabled to improve the densification of the green compact, which is consistent with literature **[~~38~~41142]**. The sintered densities of both Fe-40 vol.% YSZ and graded composite (86.7% and 90.7%, respectively) are slightly lower than those indicated in literature for a 60% YSZ reinforced austenitic stainless steel based composite **[~~29~~32333]**, for a graded YSZ reinforced steel base composite with YSZ contents in-between 20 and 90% **[~~43~~46347]** and lower or greater than those of a monolithic YSZ sintered material **[~~44~~47348]** and **[~~45~~48349]**, respectively.

#### 4.2.2.2. Reasons for uncomplete densification

With regard to the sintered Fe-40 vol.% YSZ and graded composite, their respective densities (86.7% and 90.7%) are not as high as expected ~~given~~ despite the gathered factors which should have favored their densification (§4.2.1); many reasons can explain their lack of densification, namely the work-hardening of milled powders, the sintering conditions and the competition between densification and coarsening.

*Work-hardening of powders* – The milled metallic based powder experienced work-hardening and lost some abilities to be deformed during compaction step, which explains the limited green density of the green compacts.

*Sintering conditions and sintering mechanisms* – Sintering was performed in an open matrix under a low uniaxial pressure of 50 kPa. Even if the sintering temperature and soaking time at this temperature favored the deformation of grains and diffusion leading (i) to an increase of contact areas between the powder grains and (ii) to the formation of necks entailing material densification **[~~38~~41~~42~~]**, the combined effect of temperature, soaking time and pressure did not lead to complete densification in the present work. The sintering temperature was chosen to remain slightly lower than usual sintering temperatures of YSZ **[~~41~~,45~~44~~,~~48~~45,49]** so as to maintain the nanometric distribution of reinforcements developed during milling. The soaking time was very likely insufficient as well as the sintering pressure~~. The latter parameter was~~ however chosen so as to avoid the fracture of green compacts all the more that it was applied before sintering cycle began.
With the sintering conditions and according to the microstructural observations (figure 1b and c), iron sintering has very likely proceeded at the solid state given the polygonal morphology of iron grains. In addition, the DSC signal did not reveal any endothermal transformation of iron from solid to liquid state up to 1250°C (figure 5)~~. Even if the iron grain size was nanometric in the milled powder, it did not lead to a sufficient reduction of its melting point entailing Fe melting during sintering.~~ Moreover, Fe grain growth during sintering led to submicrometric grains, which tends to confirm that Fe remained at the solid state during sintering.
Concerning iron oxides, they have very likely been sintered at the solid state except FeO which may have become liquid very locally (see figure 2u). ~~Indeed, given the promotion of phase transformations kinetics by the presence of nanometric phases, the melting of rounded shaped submicrometric FeO phase (figure 2su) may have occurred at around 1132°C (that is approximately 200°C lower than its equilibrium melting point of 1371°C **[2426]**). The value of 200°C is considered by comparison with the Feα → Feγ allotropic transformation which occurred 200°C below the equilibrium point. In the DSC signal, an endothermal but small signal has been noticed at 1132°C despite the high volume fraction of about 22% of FeO; the coarser FeO phase is indeed expected either to form a eutectic with $ZrO_2$ at 1330°C (figure 5b) very close to the equilibrium eutectic temperature of 1332°C or to melt more massively at 1330°C (figure 5b) farther than FeO equilibrium melting point of 1371°C **[2426]**.~~
An increase of sintering temperature could lead to liquid phase sintering and then to better densification.

*Competition between densification and coarsening* – Finally, t~~T~~he presence of an interconnected network of reinforcements in the sintered materials (figures 2q, r and s and 3) ~~is the last reason which~~ can explain the lack of densification. Indeed its presence confirms that ~~there has been~~ a competition occurred between composite densification and reinforcements coarsening during sintering. Coarsening of reinforcements, ~~has~~ already ~~been~~ reported in literature **[~~38~~41~~42~~]**, ~~and~~ indicates that a marked surface diffusion occurred in reinforcements at the early stages of sintering, which delays and causes harm to densification **[~~37,46~~40,~~47~~41,50]**. Coarsening can result from (i) the presence of nanometric Fe crystallites in the powder particles (figure 1a), (ii) nanoreinforcements agglomerates (figure ~~2a to o~~2a to q) with a large size distribution and eventually containing some porosities or (iii) a large ratio between grain size of matrix and reinforcements, as already reported in literature **[~~37,46,47~~40,~~49,50~~41,50,51]**. The presence of significant volume fractions of fine reinforcements of zirconia and iron oxides (figure 2 and table 1) can also favor the formation of agglomerates. According to numerical simulation results, an increase of the reinforcements volume fraction and/or a reduction of their size is shown to slow down the densification kinetics **[~~47~~50~~51~~]**. At last, the chemical nature of reinforcements can also play a role on coarsening as developed in §4.3.

### 4.3. Coarsening

In addition to the phase transformations, coarsening confirms that the milled composite powders are not thermally stable during sintering.

Firstly, YSZ reinforcements coarsened during sintering. Their size under 200 nm after milling reached a few micrometers after sintering (figure 2). As aforesaid, coarsening of oxides was predominant compared to densification during sintering, leading to the formation of an interconnected network of reinforcements. Some coarsening phenomena of zirconia have already been reported in

literature **[~~485~~52]**. Indeed grain growth of YSZ cubic phase is 30 to 250 times faster than that of tetragonal YSZ phase while a limited grain growth is observed in tetragonal YSZ phase doped with Fe and sintered at 1150°C **[~~424~~546]**. In addition to the nanometric size and the wide size distribution of reinforcements and the presence of agglomerates as already mentioned, other factors can govern the thermal stability of reinforcements. Actually, the dispersoids are thermally stable (i) if their Gibbs energy of formation is very low, (ii) if they are not soluble in the matrix and (iii) if the cation of the oxide presents a low diffusivity **[~~495~~253]**. The Gibbs energy of formation of monoclinic zirconia and FeO are respectively -1042.2 and -241.2 kJ/mol at 27°C and -818.2 et -165.8 kJ/mol at 1227°C **[11]**. No data has been found for YSZ at these temperatures in literature but it can be supposed that it presents a similar energy of formation as monoclinic zirconia, or a lower one, by comparison with other literature results **[15]**. Besides, Zr and Y are not soluble in Fe matrix **[11]**. Finally, as already mentioned, the diffusion coefficients of Zr and Y in Fe are respectively $2\times10^{-16}$ m²/s and $5\times10^{-18}$ m²/s at 977°C **[~~16~~17]**. The low Gibbs energy of formation of FeO can thus explain the coarsening and the percolation of FeO during sintering. The uncertainty about the Gibbs energy of formation of YSZ cannot enable to conclude about the YSZ thermal stability according to the previously exposed theory **[~~5~~253]**. The coarsening mechanism of oxide dispersoids is however controversial by Belyakov *et al.* who suggest that it is due to oxygen diffusion at grain boundaries **[~~505~~354]**: the oxygen diffusion, which is fast at high temperature, would indeed promote defects mobility. Oxygen ion diffuses more rapidly than cations in $ZrO_2$ and $Y_2O_3$ and very likely also in YSZ, while Fe cation diffusion is faster than that of O ion in iron oxides such as $Fe_3O_4$ and $Fe_2O_3$ **[~~283~~132]**. This mechanism could thus explain the coarsening of YSZ and $ZrO_2$ during sintering. The kinetics of coarsening is very likely increased since the reinforcements distribution is nanometric in the milled powders (figure 2) and the milled powder is nanostructured (figures 1a and 2). The high density of grain boundaries and reinforcements / matrix interfaces indeed promoted diffusion **[~~515~~455]**.

Secondly, the mean crystallites size of Fe is multiplied by a factor in-between 33 and 100 after sintering: it indeed reached 500 nm after sintering while it was close to 5-15 nm after milling (figure 1). The Fe grain growth remains however limited all the more that sintering occurs at a homologous temperature (defined as the ratio between the absolute sintering temperature and the absolute Fe melting point) of 0.84. The nanograins tend to grow with temperature because of the energy excess essentially stored in the grain boundaries **[~~515~~455]**. The high density of grain boundaries favors the diffusion processes leading to the grain growth whose driving force is all the greater that the grains are small **[~~522~~829]**. In the present study, Fe grain growth is very likely due to the weak and low pinning of grain boundaries by intergranular reinforcements (figure 1c). The latter ones experienced coarsening during sintering despite their fine distribution after milling.

### 4.4. Performances and graded feature of the bulk composite

Concerning the electrical conductivity of the bulk graded composite with all the composite subparts, it diminishes from 9.93 MS/m in Fe to 0.4 MS/m in the Fe – 40 vol.% YSZ (figure 9). According to literature, an increase of the reinforcements volume fraction **[~~53,5455,56~~56,57]**, an angular shape of reinforcements **[~~545~~657]** and/or a reduction of reinforcements size and spacing **[~~53,5555,57~~56,58]** were shown to increase the electrical resistivity of a metal matrix composite. With regard to the current results, the volume fraction, size and spacing of reinforcements are very likely the predominant factors which can explain the evolution of the electrical resistivity along the graded composite, since the reinforcements shape is similar in the various composite subparts at least at a microscopic/mesoscopic scale (figure 3). The difference of thermal expansion coefficients of the reinforcements (12-18 $\times10^{-6}$ °C$^{-1}$ for FeO from 100 to 1000°C **[~~353~~839]**, 6-8.8$\times10^{-6}$ °C$^{-1}$ for YSZ and monoclinic zirconia **[14]**) and $14.6\times10^{-6}$ °C$^{-1}$ at 800°C for the Fe matrix **[11]**) can lead to thermal stresses in the composite during the cooling stage of sintering. In addition, the $ZrO_2$ (T) → $ZrO_2$ (M) transformation of zirconia during cooling stage leads to a 3-5% volume increase entailing residual stresses and even microcracks **[~~22~~2425]**. The relief of a part of these stresses can lead to the formation of dislocations at the reinforcements-matrix interfaces. The dislocations density is all the greater that the interfaces are more numerous with the reinforcements volume fraction. Some residual stresses are moreover maintained at the reinforcements-matrix interfaces. The strain fields thus entailed in the matrix around the reinforcements constitute an energy barrier to electrons flow originating an increase

of the electrical resistivity **[~~535~~556]**. The weak electrical conductivity of oxide reinforcements, their interconnected network together with the presence of closed porosities (figure 2~~r~~t) are also expected to promote the increase of electrical resistivity of the metal matrix composite compared to pure iron.

With regard to microhardness, the gradation along the bulk material presented in figure 9 is slight and not as high as expected. The microhardness of the material depends (i) on Fe grain size, (ii) on defects density, (iii) on the porosities amount, (iv) on the quality of reinforcements/matrix interfaces and (v) on the nature and distribution of the reinforcements in terms of spacing, size and volume fraction. The global volume fraction of reinforcements was shown to increase when the YSZ content increases from 5 to 40 vol.%. This very likely increased the defects density entailed by the thermal expansion coefficient mismatch, but not necessarily decreased the Fe grain size because of the interconnected network of coarsened reinforcements. Besides, the respective hardness of FeO and $Fe_3O_4$ are 250 HV and 450 HV **[~~565~~859]**, while the respective hardness of monoclinic $ZrO_2$ and 3 mol.% yttria stabilized zirconia are 1220 HV **[14]** and 1230 to 1360 HV **[14]**. The volume fraction and the nature of reinforcements, the defects density and the porosities are very likely the predominant factors which explain the microhardness evolution along the bulk material. It is worth noting that if there had not been coarsening of reinforcements during sintering, the strengthening may have been more important and graded.

As for the 3 points bending tests, the fracture patterns display some pulled-out reinforcements and interfacial debonding (figure 10) which suggest the existence of weak bonds between the matrix and the reinforcements. In addition, the brittle and hard oxide reinforcements, which play the role of stress raisers, as well as the residual stresses, entailed during sintering by the thermal expansion coefficients mismatch between reinforcements and matrix and by the $ZrO_2$ (T) → $ZrO_2$ (M) phase transformation during cooling stage of sintering, can initiate cracks in the reinforcements and at the reinforcements-matrix interfaces. The presence of closed porosities and of an interconnected network of reinforcements can further promote the cracks propagation in the bulk material.

## 5. Conclusions

In conclusion, a graded Fe based composite strengthened with oxides hybrid reinforcements, namely tetragonal yttria stabilized zirconia, monoclinic zirconia, wüstite and at a less extent, tetragonal $Zr_{0.978}Fe_{0.0.22}O_{1.978}$ and cubic $Zr_{0.85}Y_{0.15}O_{1.93}$ was developed by high energy ball milling, uniaxial compaction and sintering. ~~Its density amounts to 90.6%.~~ The formation of wüstite very likely resulted from the reaction between $Fe_3O_4$ formed during mechanical alloying and Fe, and from the diffusion of oxygen ion from zirconia based phase towards Fe.

Sintering proceeded essentially at the solid state; some iron oxides have however very likely melted but only very locally. Sintering entailed (i) the growth of Fe grains which however remained submicrometric and (ii) the coarsening of both yttria stabilized zirconia and iron oxides reinforcements which constitute an interconnected network in the bulk graded composite, the coarsening occurring at the expense of densification (a density of 90.6% was indeed reached). ~~Some phases such as $ZrO_2$ (M), $Zr_{0.978}Fe_{0.0.22}O_{1.978}$ (T) and $Zr_{0.85}Y_{0.15}O_{1.93}$ (C) were also put into evidence in the bulk material.~~

The weak reinforcement-matrix bondings ~~is weak and~~and the porosities originated~~s~~ the low toughness and the bulk material fracture during three points bending tests. Along the bulk composite, ~~A~~a slight graded hardness was noticed as well as ~~and~~a graded electrical conductivity. ~~are finally noticed along the graded bulk composite~~ The latter one was explained by the gradation of both (i) the volume fraction, size and spacing of oxide reinforcements and (ii) the defects density.

**Aknowledgments**

The authors are very thankful to P. Roussel, UCCS, Lille University, France for having performed the in-situ X-ray diffractometry experiment, to D. Troadec from IEMN, Lille, France for the preparation of thin foils by FIB, to the Microscopy platform of Lille University, France for the use of electron microscopes, to Ch. Vermander, Ecole Centrale de Lille, France for the numerous dies and pistons machining required for compaction and sintering, and to S. Shihab, Laboratoire d'électrotechnique et

d'électronique de puissance, Lille University, France for his help in measurement of electrical conductivity. K. Naji is grateful to ANRT (French National Association of Research and Technology) for her financial support under CIFRE convention n° 2014/1316.

## References

[1] M.-N. Avettand-Fènoël, R. Taillard, J. Dhers, J. Foct, Effect of Ball Milling Parameters on the Microstructure of W-Y Powders and Sintered Sample, International Journal of Refractory Metals and Hard Materials 21 (2003) 205-213

[2] M.-N. Avettand-Fènoël, R. Taillard, J. Dhers, J. Foct, Evolution of grain size in oxide dispersion strengthened tungsten alloys during their elaboration by ball milling and sintering, International Journal of Nanotechnology, 5, Nos. 6/7/8 ( 2008) Eds. F. Grasset, Ph. Goudeau 669-682

[3] A. Anghelus, M.-N. Avettand-Fènoël, C. Cordier, R. Taillard, Microstructural evolution of aluminium/Al-Ni-Sm glass forming alloy laminates obtained by controlled accumulative roll bonding, Journal of Alloys and Compounds 631 (2015) 209-218

[4] J.S. Carpenter, S. Zheng, R. Zhang, S.C. Vogel, I.J. Beyerlein, N.A. Mara, Thermal stability of Cu-Nb nanolamellar composites fabricated via accumulative roll bonding, Philosophical magazine A 93(7) 718-735

[5] C. Suryanarayana, N. Al-Aqeeli, Mechanically alloyed nanocomposites, Progress in Materials Science 58 (2013) 383-502

[6] V. Viswanathan, T. Laha, K. Balani, A. Agarwal, S. Seal, Challenges and advances in nanocomposite processing techniques, Materials Science and Engineering R54 (2006) 121-285

[7] S.C. Tjong, Z.Y. Ma, Microstructural and mechanical characteristics of in situ metal matrix composites, Materials Science and Engineering 29 (2000) 49-113

[8] A. Bachmaier, R. Pippan, Generation of metallic nanocomposites by severe plastic deformation, International Materials reviews 58(1) (2013) 41-62

[9] V. Sharma, U. Prakash, B.V. Manoj Kumar, Surface composites by friction stir processing: a review, Journal of Materials Processing and Technology 224 (2015) 117-134

[10] J.J. Sobczak, L. Drenchev, Metallic functionally graded materials: a specific class of advanced composites, J. Mater. Sci. Technol. 29(4) (2013) 297-316

[11] Smithells Metals Reference Book, 7th edition, Eds: E.A. Bra,des, G.B. Brook, Butterworth Heinemann, Oxford, 1992

[12] Techniques de l'ingénieur – Gilles Greffier – 1996 – Matériaux pour résistance électrique

[13] J. Robert Kelly, I. Denry, Stabilized zirconia as a structural ceramic: an overview, Dental Mater. 24 (2008) 289-298

[14] CES Edupack, Granta Design Limited, Cambridge, 2008

[15] T. Maeda, S. Ukai, S. Hayashi, N. OOno, Y. Shizukawa, K. Sakamoto, Effects of zirconium and oxygen on the oxidation of FeCrAl-ODS alloys under air and steam conditions up to 1500°C, Journal of Nuclear Materials 516 (2019) 317-326

[~~15~~16] A. Sari, M. Keddam, A. Guittoum, Effect of iron impurity on structural development in ball-milled $ZrO_2$-3mol% $Y_2O_3$, Ceramics International 41 (2015) 1121-1128

[~~16~~17] D. Murali, B.K. Panigrahi, M.C. Valsakumar, C.S. Sundar, Diffusion of Y and Ti/Zr in bcc iron : A first principles study, Journal of nuclear materials 419 (2011) 208-212

[~~17~~18] P. Perrot, Iron-Oxygen-Yttrium, Iron Systems: Phase Diagrams, Crystallographic and Thermodynamic Data, Landolt-Börnstein, New series IV/11D5, MSIT, Springer 2009

[~~18~~19] O. Fabrichnaya, Iron-Oxygen-Zirconium, Iron Systems: Phase Diagrams, Crystallographic and Thermodynamic Data, Landolt-Börnstein, New series IV/11D5, MSIT, Springer 2009

[20] R.E. Reed-Hill, Physical Metallurgy Principles, 2nd edition, D. Van Nostrand Company, New York, 1973

[~~1920~~21] NF ISO 5017 May 2013, Dense shaped refractory products - Determination of bulk density, apparent porosity and true porosity - Produits réfractaires façonnés denses, AFNOR, May 2013

[~~2021~~22] NF EN ISO 14125, Détermination des propriétés de flexion des composites, 1998

[~~2122~~23] D.K. Schroder, Semiconductor Material and Device Characterization, 3rd Edition (2015)

[~~23~~24] C. Papandrea, L. Battezzati, A Study of the α<-->γ Transformation in Pure Iron: Rate Variations Revealed by Means of Thermal Aanlysis. Philos. Mag. 87 (2007) 1601–1618.

[~~2224~~25] J. Chevalier, L. Gremillard, A .V. Virkar, D.R. Clarke, The tetragonal- monoclinic transformation in zirconia: lessons learned and future trends, J. Am. Ceram. Soc., 92(9) (2009) 1901-1920

[~~2325~~26] M. Gauna, S. Conconi, S. Gomez, G. Suarez, E.F. Aglietti, N.M. Rendtorff, Monoclinic-tetragonal zirconia quantification of commercial nanopowder mixtures by XRD and DTA, Ceramics Silikaty 59(4) (2015) 318-325

[~~2426~~27] S.V. Bechta, E.V. Krushinov, V.I. Almjashev, S.A. Vitol, L.P. Mezentseva, Yu.B. Petrov, D.B. Lopukh, V.B. Khabensky, M. Barrachin, S. Hellmann, K. Froment, M. Fischer, W. Tromm, D. Bottomley, F. Defoort, V.V. Gusarov, Phase diagram of the $ZrO_2$–FeO system, Journal of Nuclear Materials 348 (2006) 114–121

[~~2527~~28] P. Jha, P. Gupta, D. Kumar, O. Parkash, Effect of sintering mechanism on the properties of $ZrO_2$ reinforced Fe metal matrix nanocomposite, Journal of composites, 2015 (2015) ID 456353, 8p

[~~5228~~29] L. He, E. Ma, Nanophase metallic alloys consolidated from powders prepared by mechanical alloying, Materials Science and Engineering A204 (1995) 240-245

[~~2629~~30] P. Jha, P. Gupta, D. Kumar, O. Parkash, Synthesis and characterization of Fe-$ZrO_2$ metal matrix composites, Journal of Composite Materials 48(17) (2014) 2107-2115

[~~2730~~31] M. Wildan, H.J. Edrees, A. Hendry, Ceramic matrix composites of zirconia reinforced with metal particles, Materials Chemistry and Physics 75 (2002) 276-283

[~~2831~~32] A. Atkinson, Chapter 6: Diffusion in Ceramics, Materials Science and Technology, Wiley (2006) 297-337

[~~2932~~33] J. Tarabay, V. Peres, E. Serris, F. Valdivieso, M. Pijolat, Zirconia matrix composite dispersed with stainless steel particles: processing and oxidation behavior, Journal of the European Ceramic Society 33 (2013) 1101-1110

[~~3033~~34] J. Philibert, A. Vignes, Y. Bréchet, P. Combrade, Métallurgie, du minerai au matériau, Masson, Paris, 1998

[~~3134~~35] T. Yamashita, P. Hayes, Analysis of XPS spectra of $Fe^{2+}$ and $Fe^{3+}$ ions in oxide materials, Applied surface science 254 (2008) 2441-2449

[~~3235~~36] G. Becgta, W. Weiss, W; Ranke, R. Schlögl, Bulk and surface phases of iron oxides in an oxygen and water atmosphere at low pressure, Phys. Chem. Chem. Phys. 3 (2001) 1114-1122

[~~3336~~37] T.-C. Lin, G. Seshadri, J.A. Kelber, A consistent method for quantitative XPS peak analysis of thin oxide films on clean polycrystalline iron surfaces, Applied Surface Science 119 (1997) 83-92

[~~3437~~38] D.G. Isaak, R.E. Cohen, M.J. Mehl, D.J. Singh, Phase stability of wüstite at hogh pressure from first-principles linearized augmented plane-wave calculations, Physical Review B 47, 7720 (1993)

[~~3538~~39] M. Takeda, T. Onishi, S. Nakakubo, S. Fujimoto, Physical properties of iron-oxide scales on Si-containing steels at high temperature, Materials Transactions 50(9) (2009) 2242-2246

[~~3639~~40] X. Yang, Z. Ni, X. Xu, J. Yang, Novel preparation of anto-static zirconia ceramic by iron infiltration at high temperature, Ceramics International 43 (2017) 1227-1230

[~~3740~~41] W.H. Rhodes, Agglomerate and particle size effects on sintering yttria-stabilized zirconia, Journal of the American ceramic society 64(1) (1981) 19-22

[~~3841~~42] R.M. German, Sintering Theory and Practice, John Wiley & Sons, Inc., New York, 1996.

[~~3942~~43] G.C.T. Silva, E.N.S. Muccillo, Effect of Co addition on sintering and electrical properties of yttria stabilized zirconia, Sixth international latin-american conference on powder technology, November 07-10, Buzios, Brazil (2008) 692-697

[~~4043~~44] J.L. Shi, T.S. Yen, H. Schubert, Effect of small amounts of additives on the sintering of high-purity Y-TZP, Journal of materials science 32 (1997) 1341-1346

[~~4144~~45] P. Satardekar, D. Montinaro, V.M. Sglavo, Fe-doped YSZ electrolyte for the fabrication of metal supported-SOFC by co-sintering, Ceramics International 41 (2015) 9806-9812

[~~4245~~46] F. Guo, P. Xiao, Effect of $Fe_2O_3$ doping on sintering of yttria-stabilized zirconia, Journal of the European ceramic Society 32 (2012) 4157-4164

[~~4346~~47] Y.G. Jung, S.C. Choi, C.S. Oh, U.G. Paik, Residual stress and thermal properties of zirconia/metal (nickel, stainless steel 304) functionally graded materials fabricated by hot pressing, Journal of Materials Science 32 (1997) 3841-3580

[~~4447~~48] A. Kato, K. Inoue, Y. Katatae, Sintering behavior of yttria-stabilized zirconia (YSZ) powders prepared by homogeneous precipitation, Mat. Res. Bull., 22 (1987) 1275-1281

[~~4548~~49] H.L. Chu, C.L. Wang, H.E. Lee, Y.Y. Sie, R.S. Chen, W.S. Hwang, M.C. Wang, Effect of sintering process parameters on the properties of 3Y-PSZ ceramics, IOP Conf. Series: Materials Science and Engineering 47 (2013) 012005

[~~4649~~50] Maschio, O. Sbaizero, S. Meriani, Sintering aids for ceria-zirconia alloys, Journal of Materials Science 27 (1992) 2734-2738

[~~4750~~51] Z. Yan, C.L. Martin, O. Guillon, D. Bouvard, Effect of size and homogeneity of rigid inclusions on the sintering of composites, Scripta Materialia 69 (2013) 327-330

[~~4851~~52] D. Casellas, M.M. Nagl, L. Llanes, M. Anglada, Microstructural coarsening of zirconia toughened alumina composites, J. Am. Ceram. Soc. 88(7) (2005) 1958-1963

[~~4952~~53] U. Grundman, M. Heilmaier, U. Martin, H. Oettel, L. Schultz, Oxide dispersion strengthened silver : manufacturing and properties, Zeitschrift für Metallkunde 94(5) (2003) 587-592

[~~5053~~54] A. Belyakov, Y. Sakai, T. Hara, Y. Kimura, K. Tsuzaki, Annealing behavior of submicrocrystalline oxide-bearing iron produced by mechanical alloying, Met. Mater. Trans. 34A (2003) 131-138

[~~5154~~55] H. Gleiter, Nanostructured materials: basic concepts and microstructure, Acta Materialia 48 (2000) 1-29

[~~5355~~56] S.-Y. Chang, C.-F. Chen, S.-J. Lin, T.Z. Kattamis, Electrical resistivity of metal matrix composites, Acta materialia 51 (2003) 6191-6302

[~~5456~~57] L. Weber, J. Dorn, A. Mortensen, On the electrical conductivity of metal matrix composites containing high volume fractions of non-conducting inclusions, Acta Materialia 51 (2003) 3199-3211

[~~5557~~58] A.L. Lima, X. Zhang, A. Misra, C.H. Booth, E.D. Bauer, M.F. Hundley, Length scale effects on the electronic transport properties of nanometric Cu/Nb multilayers, Thin solid films 515 (2007) 3574-3579

[~~5658~~59] Guide de sous traitance des traitements de surface et de la peinture industrielle, Jean Chevalier, Lavoisier, Ed Tec & Doc, Paris, 2012s